Soft Matter

PAPER

View Article Online
View Journal | View Issue

Cite this: *Soft Matter*, 2017, **13**, 8451

New insights into the flow and microstructural relaxation behavior of biphasic cellulose nanocrystal dispersions from RheoSANS

Alexander D. Haywood,[a] Katie M. Weigandt,[b] Partha Saha,[a] Matthew Noor,[a] Micah J. Green [c] and Virginia A. Davis *[a]

Received 5th April 2017,
Accepted 15th October 2017

DOI: 10.1039/c7sm00685c

rsc.li/soft-matter-journal

Cellulose nanocrystals (CNC) have been studied as nanostructured building blocks for functional materials and function as a model nanomaterial mesogen for cholesteric (chiral nematic) liquid crystalline phases. In this study, both rheology and small angle neutron scattering (RheoSANS) were used to measure changes in flow-oriented order parameter and viscosity as a function of shear rate for isotropic, biphasic, liquid crystalline, and gel dispersions of CNC in deuterium oxide (D_2O). In contrast to plots of viscosity *versus* shear rate, the order parameter trends showed three distinct rheological regions over a range of concentrations. This finding is significant because the existence of three rheological regions as a function of shear rate is a long-standing signature of liquid crystalline phases composed of rod-like polymers, but observing this trend has been elusive for high-concentration dispersions of anisotropic nanomaterials. The results of this work are valuable for guiding the development of processing methodologies for producing ordered materials from CNC dispersions and the broader class of chiral nanomaterial mesogens.

Introduction

In the last ten to twenty years, the scalable production of anisotropic nanomaterials has spurred a "New Era"[1] in liquid crystal research.[2] This "New Life from Old Roots"[3] is based on increasing recognition that the processing lyotropic liquid crystalline dispersions of anisotropic nanomaterials is a scalable and cost effective approach for producing large oriented materials from anisotropic nanomaterials.[3,4] For example, there is considerable interest in understanding and processing lyotropic dispersions of cellulose nanocrystals (CNC) to produce coatings and films with anisotropic mechanical and/or optical properties.[5–15] CNC are an intriguing building block for advanced materials due to their natural abundance, low density, 150 GPa Young's Modulus,[16] and increasing commercial availability. Several researchers have used unidirectional shear of CNC dispersions to prepare aligned CNC coatings and films.[9,17–19] In addition, magnetic fields,[20] rotational shear,[21] and simple evaporation[7] have been used to prepare CNC films with chiral microstructures.[2] Although they are not truly cylindrical, CNC extracted from biomass using sulfuric acid hydrolysis are known to exhibit the lyotropic liquid crystalline phase behavior associated with "rod-like" mesogens. At low concentrations, CNC dispersions are isotropic. Assuming that points of nucleation are present, the system will become biphasic above a threshold (binodal) volume fraction ϕ_I, such that a liquid crystalline phase forms in equilibrium with the isotropic phase. (The transition is pushed to a higher, spinodal point if nucleation does not occur.) Above the biphasic–nematic binodal concentration ϕ_{LC}, the system becomes fully liquid crystalline. These transitions are essentially due to the same balance of rotational and translational entropy first described by Onsager.[22] As for other chiral macromolecular mesogens such as the rod-like polymers poly-γ-benzyl-L-glutamate (PBLG) and hydroxypropyl cellulose (HPC), CNC dispersions form cholesteric (chiral nematic) liquid crystals where the mesogens rotate along a helical axis. The application of shear or other external fields to CNC dispersions can result in annealing of defects and unwinding of the cholesteric pitch to form a nematic-like structure where the CNC are all aligned parallel to the flow direction. In the last few years, there has been a growing body of work on the rheology of lyotropic CNC dispersions, but fundamental understanding of the rheophysics is at a very nascent stage compared to the detailed theoretical understanding that has been achieved for more established systems such as rod-like polymers[23–33] and

[a] *Department of Chemical Engineering, Auburn University, Auburn, Alabama 36849, USA. E-mail: davisva@auburn.edu; Tel: +1 334 844 2060*
[b] *Center for Neutron Research, National Institute of Standards and Technology, Gaithersburg, Maryland 20899, USA*
[c] *Artie McFerrin Department of Chemical Engineering, Texas A&M University, College Station, TX, USA*

worm-like micelles.[34–36] While CNC can be considered colloidal rods, their rheology and phase behavior is more complex than that of monodisperse attractive rods such as fd virus which have been the subject of detailed experimental and computational studies.[37] Differences in the biomass source used, details of the CNC extraction protocol, type of counter-ion, and other experimental parameters between studies have resulted in differences in the rheological properties and liquid crystalline phase transitions obtained by different researchers.[6,11,38–45] Nonetheless, multiple studies have shown that CNC dispersions have two significant distinctions from the empirical behavior and theoretical understanding established for lyotropic rod-like polymer solutions.

First, CNC dispersions do not exhibit a maximum in the biphasic region of the viscosity *versus* concentration curve. For lyotropic rod-like polymers, the low shear viscosity increases with concentration until the majority of the dispersion is liquid crystalline; it then decreases with concentration reaching a minimum when the sample becomes fully liquid crystalline at ϕ_{LC} and then increases, often dramatically, at higher concentrations. However, for charged mesogens such CNC, chitin,[46] and halloysite,[47] viscosity increases with concentration. While this behavior is not fully understood, it is generally attributed to electroviscous effects and the mesogen concentrations in the liquid crystalline and isotropic phases being a function of total concentration in accordance with Stroobants–Lekkerkerker–Odijk (SLO) theory.[48,49]

Second, viscosity *versus* shear rate curves sometimes show three regions for biphasic, but not liquid crystalline, CNC dispersions; there is a shear thinning region, a nearly Newtonian plateau, and then a second shear thinning region. Three-region viscosity *versus* shear rate curves are relatively well understood for nematic rod-like polymer liquid crystalline solutions. However, some cholesteric systems such as PBZT do not adhere well to theory,[50] and even the thoroughly investigated HPC is being revisited.[51] In the case of fully liquid crystalline nematic dispersions of several nanomaterial mesogens, clear identification of three-region behavior has been elusive.[52–55] As recently pointed out by Carreau and coworkers, the three-region behavior sometimes observed in CNC dispersions has generally been attributed to the same origins as in fully liquid crystalline dispersions of rod-like polymers, but this has never been verified.[50] It is unexpected that the viscosity *versus* shear rate curves for biphasic CNC dispersions have three regions while the fully liquid crystalline dispersions are continuously shear thinning. These experimental results are not readily explained based on the theories developed for lyotropic rod-like polymer dispersions.

The goal of this research was to combine rheology and small angle neutron scattering (RheoSANS) to gain new insights into the shear induced microstructural changes in CNC dispersions. RheoSANS has made valuable contributions to understanding a range of complex fluids;[56] this is particularly true in the case of worm-like micelles. Worm-like micelles are a particularly complex type of lyotropic dispersions. Unlike solid mesogens such as CNC, flow can result in fusion (or breakage) of worm-like micelles thereby changing the phase boundaries, which necessitates creation of non-equilibrium phase diagrams.[35,36,56,57] In contrast to worm-like micelles there is a paucity of literature on RheoSANS of CNC dispersions.[58,59] Orts *et al.* used RheoSANS to study the effect of aspect ratio (and geometric polydispersity) on the flow-induced alignment of CNC dispersions, with particular emphasis on fully liquid crystalline dispersions. They observed a transition from a cholesteric to a nematic-like microstructure during flow.[58,59] Similarly, Ebeling *et al.*'s combined rheology and small-angle X-ray scattering investigation (RheoSAXS) found enhanced ordering with flow for 4.4 vol% (6.9 wt%) liquid crystalline CNC dispersions.[60] However, contrary to Orts *et al.*, Ebeling *et al.* observed alignment in the vorticity direction at low shear rates. This was attributed to either the alignment of planes within the polydomain structure of the liquid crystal, or end-over-end tumbling of the nanocrystals.[60]

In this work, the combination of microscopy, rheology, and RheoSANS was used to investigate dispersions of CNC in D_2O for isotropic, biphasic, liquid crystalline and gel dispersions. In contrast to the laboratory-extracted CNC from cotton used by Orts and Ebeling, this research used the ion-exchanged CNC extracted from woody biomass that only recently became available in pilot plant quantities. The results of this research provide new insights into the microstructural changes that contribute to CNC's unusual rheological behavior and provide a foundation for future work.

Experimental section

Materials

Freeze dried cellulose nanocrystals (CNC) produced by the sulfuric acid hydrolysis of woody biomass were obtained from the US Forest Service's Cellulose Nanomaterials Pilot Plant at the Forest Products Laboratory (Lot # 2012-FPL-CNC-051). Based on atomic force microscopy measurements (AFM) using a Pacific Nanotechnology Nano-R SPM, the average CNC length was 163 nm with a standard deviation (σ) of 43 nm, the average width was 33 nm (σ = 7.2 nm), and the average height was 6.3 nm (σ = 1.6 nm). Approximately 10 μL of 0.05 vol% CNC was pipetted onto a freshly cleaved mica surface. The dispersion was allowed to sit for 5 minutes on the mica surface, which was then blown dry with dry air, leaving behind adsorbed CNC on the surface. The AFM was operated in noncontact mode. Each 5 μm^2 area scan was acquired at a scan speed of 0.25 Hz with a 1024 × 1024 pixel resolution. To enable width measurement, an image of the tip was obtained using a porous aluminum standard surface and Gwyddion's blind tip estimation algorithm; the tip image was used to deconvolute the shape of the particles from the image of the tip.

Deuterium oxide (D_2O) (99.8 atom %) was obtained from Acros Organics (viscosity 1.74 mPa s at 10 °C). A vortex mixer was used to mix approximately 12 g of CNC and 88 g of D_2O. The mixture was then placed in an ice bath and sonicated using a Sonics VC750 ultrasonic processor at 60% amplitude for a total of 35 minutes in 5 cycles of 7 minutes on and 2 minutes off.

The mixture was stirred by hand during the off cycles. The resulting CNC concentration was 12.0 wt% CNC based on thermogravimetric analysis (TGA). Using the densities of crystalline cellulose and D_2O at 25 °C, which are 1.64 and 1.11 g ml^{-1}, respectively this equates to ϕ = 8.48 vol%. This dispersion was then diluted with D_2O and thoroughly mixed to result in dispersions with the desired concentrations. The 10 samples investigated in this work were 2.49, 3.16, 3.83, 5.16, 5.83, 6.50, 7.16, 7.82, and 8.48 vol%.

Polarized optical microscopy

A droplet of each dispersion was sandwiched between a microscope slide and cover slip using a SecureSeal Imaging Spacer with a 0.12 mm well depth. Images were taken using a Nikon Eclipse 80i with an LU Plan Fluor 20×/0.45NA Nikon objective lens and a Nikon DS-Ri2 camera. All images were taken between crossed polarizers. For sheared CNC dispersions, the microscope was equipped with a Linkam CSS450 Optical Rheology Stage. These images were taken at room temperature with an L Plan SLWD 20×/0.35NA Nikon objective lens. Crossed polarizers were used for all images with the shearing direction oriented at 0° or 45° with respect to the polarization axis, as indicated.

Rheological measurements

Rheological measurements were obtained for dispersions with CNC concentrations ranging from 2.49 vol% to 8.48 vol% using an Anton Paar MCR301 rotational rheometer and our previously described protocols.[39] Since small changes in concentration can cause large variations in rheological properties, measurements were made at 10 °C and an evaporation blocker was used. For low viscosity samples (2.49–4.50 vol%), a Mooney–Ewart geometry (21.0 mm bob diameter, 22.2 mm cup inner diameter, and 52.0 mm gap length) was typically used. For higher viscosity samples (5.16–8.48 vol%) a cone and plate geometry (50.0 mm diameter and 2.018° cone angle) was typically used. Some samples were tested in both fixtures to ensure the absences of fixture related artifacts.

Oscillatory measurements at a fixed frequency of 10 rad s^{-1} and amplitudes from 0.01% to as much as 40% strain were performed to determine the linear viscoelastic regime; this was followed by frequency sweeps from 0.01 to 100 rad s^{-1} at an amplitude within the linear viscoelastic regime for that sample. In addition, successive amplitude sweeps were performed within the linear viscoelastic regime to ensure that the sample microstructures were stable against evaporation, or phase separation over the time scale of testing. Steady shear viscosity *versus* shear rate curves were generated from 0.01 to 100 s^{-1} for each sample. The time to steady shear for each concentration was determined by a start-up flow test at 0.01 s^{-1}, the sample time was then decreased linearly with increasing shear rate to a minimum time of 50 s at 100 s^{-1}. Some points for the low concentration dispersions were below the sensitivity of the torque transducer; these points are not shown in the figures.

RheoSANS

Neutron scattering experiments were conducted on the NGB 30 m and NGB 10 m small angle neutron scattering (SANS) beam lines at the NIST Center for Neutron Research in Gaithersburg, MD. A low concentration dilution series was measured on the 10 m SANS in standard titanium demountable cells. For flow experiments, the NGB 30 m instrument was configured with 6 Å neutron wavelength and a sample to detector distance of 8.5 m. For samples at rest, two additional configurations were used; 6.0 Å neutron wavelength and sample to detector distance of 1.9 m, and 8.4 Å neutron wavelength and sample to detector distance of 13.7 m. The sample environment was an Anton Paar MCR501 rotational rheometer with a titanium cup and hollow bob (48.0 mm bob diameter and 50.0 mm cup internal diameter) specifically designed for SANS measurement compatibility. Rectangular apertures 18 mm by 10 or 0.25 mm were used for radial and tangential measurements respectively. All measurements were performed at 10 °C. Measurements were performed through both the radial and tangential directions in order to probe the microstructure in the flow-vorticity and gradient-vorticity planes, respectively. The scattering data were reduced to an absolute scale using the standard NIST Igor procedures.[61] Due to the complicating effects of the curved transmission path in the tangential configuration, the tangential scattering data were scaled to match the absolute radial scattering intensity in the common (vorticity) direction.

Results and discussion

Phase behavior and viscoelasticity

Much of the previous research on CNC rheology and phase behavior was based on small batches of sulfonated CNC extracted from cotton dispersed in water with H^+ as the counterion. More recently, a variety of CNC from several industry and government pilot plants has become available.[62] This research used freeze-dried CNC from the US Forest Products Lab's pilot plant. These CNC were extracted from woody biomass, and underwent an ion exchange process to replace H^+ with Na^+ as the counterion.[62] These differences and the use of D_2O of the solvent necessitated using a combination of rheology and cross-polarized optical microscopy to determine the phase boundaries and rheological properties prior to performing RheoSANS.[39,42] As expected, increasing concentration caused the dispersions to transition from isotropic, to biphasic, to liquid crystalline, to rheological gels. Fig. 1 shows cross-polarized optical microscope images of dispersions with CNC concentrations ranging from 3.16 to 8.48 vol%. Fig. 2 shows the viscoelastic properties of these dispersions: storage modulus G', loss modulus G'', tan $\delta = G''/G'$, and complex viscosity η^*. Results from 2.49 vol% CNC dispersions are not shown; they were isotropic and lacked appreciable viscoelasticity. At 3.16 vol%, a few small liquid crystalline droplets were dispersed in a predominant continuous isotropic phase (Fig. 1), indicating the isotropic to biphasic transition concentration $\phi_I \approx$ 3.16 vol%. At 3.83 vol%, the number of liquid crystalline droplets in the

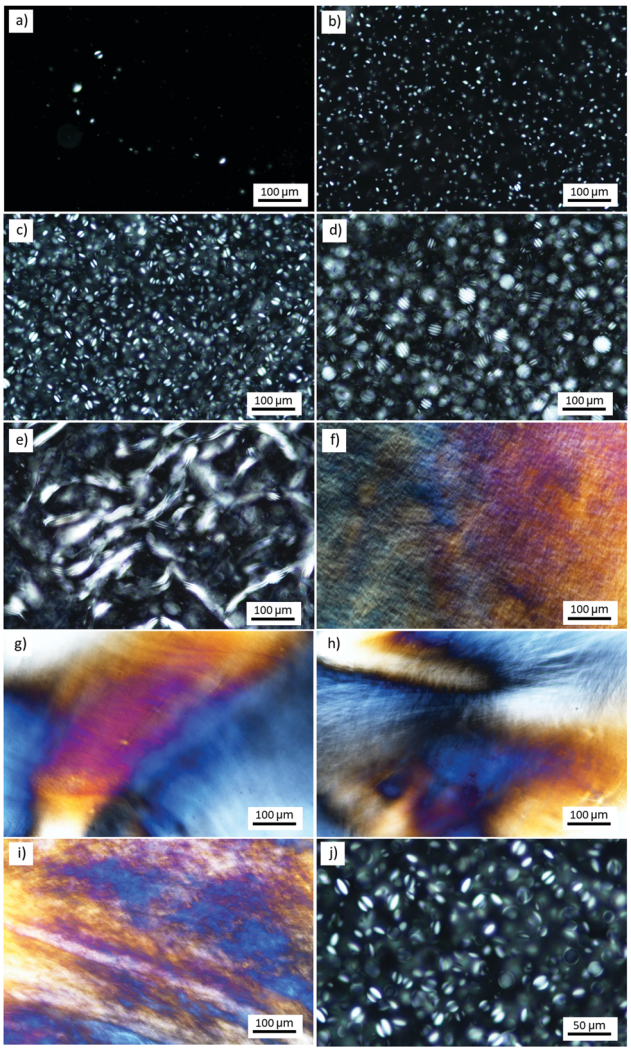

Fig. 1 Polarized optical microscopy images of CNC dispersions at (a) 3.16, (b) 3.83, (c) 4.50, (d) 5.16, (e) 5.83, (f) 6.50, (g) 7.16, (h) 7.82, and (i) 8.48 vol%. In (j) the 4.50 vol% image from (c) is magnified to clearly show the texture of the liquid crystalline droplets.

dispersion significantly increased. As the concentration was further increased, the fraction of liquid crystalline phase increased and the anisotropic droplets became larger. Between 3.83 and 5.83 vol%, the dispersions had the layer-like striped disclination pattern typical of cholesteric droplets with perpendicular surface anchoring,[63] but isotropic regions were visible and the dispersions were predominantly viscous ($\tan\delta > 1$). The combination of microscopy and rheology indicates that these dispersions were biphasic with a co-continuous matrix of isotropic and liquid crystalline phases. In contrast, the 6.50 vol% dispersion was primarily elastic ($\tan\delta < 1$) and cross-polarized microscopy images were completely birefringent with a variety of interference colors. This indicates the dispersions became fully liquid crystalline at $\phi_{LC} \approx 6.50$ vol%. Interestingly, none of the dispersions exhibited the characteristic fingerprint pattern of single-phase cholesteric liquid crystals including aqueous dispersions of the same batch of sulfonated CNC. At 7.16 vol%,

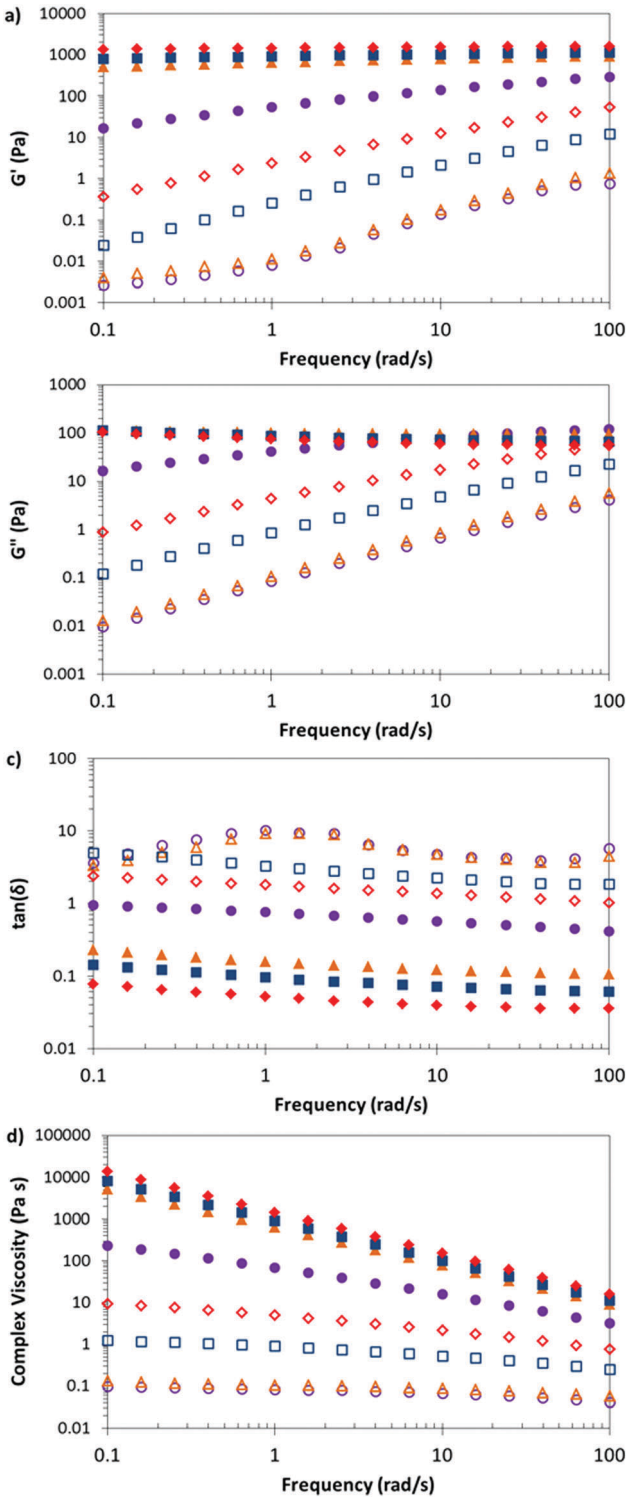

Fig. 2 Linear viscoelastic properties of CNC dispersions at 3.83 vol% (purple open circles), 4.50 vol% (orange open triangles), 5.16 vol% (blue open squares), 5.83 vol% (red open diamonds), 6.50 vol% (purple solid circles), 7.16 vol% (orange solid triangles), 7.82 vol% (blue solid squares), and 8.48 vol% (red solid diamonds). Data is the average of four tests.

the dispersions were more colorful, there was a significant decrease in $\tan\delta$, and the G' was independent of ω indicating that $\phi_{GEL} \approx 7.16$ vol%. However, only the 8.48 vol% sample

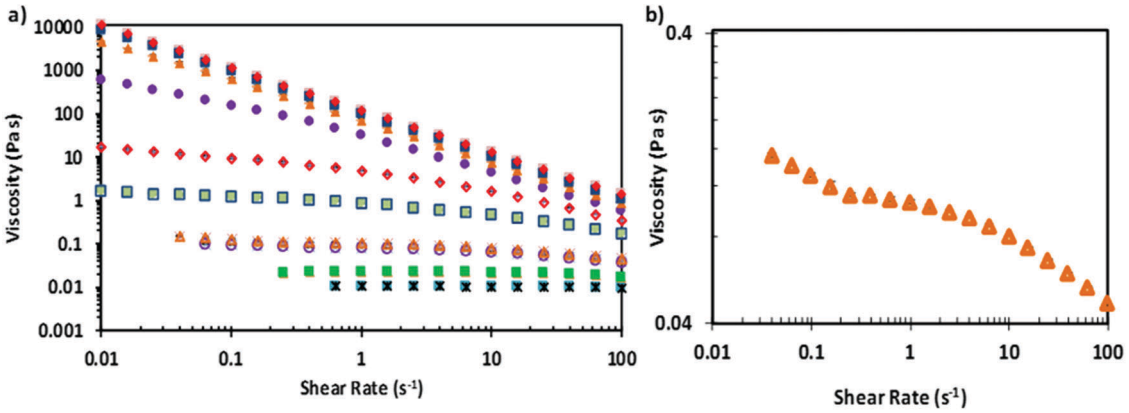

Fig. 3 (a) Viscosity *versus* shear rate for 2.49 vol% (black stars), 3.16 vol% (green closed squares), 3.83 vol% (purple open circles), 4.50 vol% (orange open triangles), 5.16 vol% (blue open squares), 5.83 vol% (red open diamonds), 6.50 vol% (purple solid circles), 7.16 vol% (orange solid triangles), 7.82 vol% (blue solid squares), and 8.48 vol% (red solid diamonds). (b) 4.50 vol% dispersion showing three regions. Data is the average of four tests, error bars are smaller than symbol size.

exhibited the watercolor texture typically associated with lyotropic gels.[64] It is noted that in our previous work, using CNC from cotton dispersed in water with H^+ as a counterion $\phi_{LC} \approx 12.4$ vol% and $\phi_{GEL} \approx 14.5$ vol%. The significant difference in the phase boundaries highlights the significant effects differences in CNC source, counterion, and solvent can have on phase behavior.[44,50]

Steady shear rheology

The steady shear rheology of dispersions of CNC in D_2O (Fig. 3) shows similar behavior to our previous investigations of CNC in H_2O.[39,42] For rheologically dilute dispersions of rods, the rotational diffusion coefficient D_{ro} is

$$D_{ro} = \frac{3k_BT(\ln(L/d) - 0.8)}{\pi\eta_s L^3} \quad (1)$$

η_s is the solvent viscosity, L is the length, k_B is Boltzmann's constant, T is the temperature and d is the diameter.[24] At higher concentrations, an effective rotational diffusivity scale can be determined $D_r^{eff} \propto D_{ro}/\phi^2$; even in the semidilute regime the proportionality constant is on the order of 10^3–10^4. For higher concentrations, D_r^{eff} is obtained as a function of the order parameter and D_r at a reference concentration.[24] For the CNC in D_2O at 10 °C, $D_{ro} \approx 400$ s^{-1}; the corresponding relaxation time $\tau = 0.006$ s. Since dilute Brownian rods begin to shear thin when the Weissenberg number $Wi = \tau\dot{\gamma} > 0.2$,[65] shear thinning was not observed in the experimental range of 0.01 to 100 s^{-1}. The lack of shear thinning can also be viewed in terms of the Peclet number or the ratio of shear to Brownian forces $Pe = \dot{\gamma}/D_{ro}$ being less than 1 below 400 s^{-1}. Therefore it is not surprising that low concentration dispersions were essentially Newtonian. In fact, even the 2.49 vol% dispersion was nearly Newtonian (Fig. 3). At 3.16 vol%, the approximate onset of the biphasic regime, the dispersions began to exhibit shear thinning. The onset of shear thinning near the onset of the biphasic regime is likely related to the collective rotational diffusion critically slowing down near the isotropic nematic transition.[66] Lonetti *et al.* (2008) analyzed this behavior in detail for long, thin rods with repulsive interactions that exist over smaller range than the length of the rod. However, understanding the details of the CNC's rheological behavior is complicated by their non-cylindrical geometry, polydispersity, and electroviscous effects. Shear thinning behavior is defined by $\eta = K\dot{\gamma}^{n-1}$; where η = viscosity, $\dot{\gamma}$ is the shear rate, K is the consistency coefficient related to temperature and n is the rate index. A value of $n = 1$ is equivalent to Newtonian behavior, $n < 1$ indicates shear thinning, $n = 0$ indicates yielding, and $n > 1$ indicates shear thickening. As shown in Table 1 the power law rate indices n over the lowest ($0.01 \leq \dot{\gamma} \leq 0.1$ s^{-1}) and highest ($10 \leq \dot{\gamma} \leq 100$ s^{-1}) were different. This suggests the possibility of the three-region behavior first identified by Onogi and Asada[19] that is a known characteristic of many lyotropic liquid crystalline systems.[23,67,68] The physical origins of three-region behavior are well understood for nematic liquid crystals comprised of rod-like polymers. In region I, at low shear, the polydomain structure is not altered but shear thinning results from domains sliding past each other.[51] In region II, at intermediate shear rate, the system is in a transition state. In region III, at high shear rate, the samples shear thin due to flow alignment of the mesogens. However, in the case of several nematogenic and cholesterogenic nanomaterial mesogens clearly identification of three-region behavior has been elusive.[2,39,52,53,55,69,70]

Table 1 Calculated power law rate indices (n) for CNC dispersions at low (0.01–0.1 s^{-1}) and high (10–100 s^{-1}) shear rates

CNC conc. (vol%)	n (low $\dot{\gamma}$)	n (high $\dot{\gamma}$)
3.83	0.92	0.77
4.50	0.84	0.77
5.16	0.80	0.58
5.83	0.74	0.36
6.50	0.41	0.12
7.16	0.14	0.05
7.82	0.06	0.02
8.48	0.01	0.06

Furthermore, the shear response of cholesteric dispersions is more complex than that of nematic dispersions since shear can induce unwinding of cholesteric pitch to a nematic-like microstructure. In the case of CNC, several research groups have observed three regions in viscosity *versus* shear rate curves for CNC dispersions.[6,39,40,50] For example, Ureña-Benavides *et al.*[39] concluded based on visual inspection that three-region behavior existed only in the biphasic region, while Orts *et al.* identified three-region behavior for only liquid crystalline CNC.[58] As pointed out by Carreau and coworkers, even though CNC flow behavior is currently being explained in terms of the framework first described by Onogi and Asada, the origin is not yet confirmed.[50] A better understanding of the effects of shear on the cholesteric phase is needed.[50] In addition to being of fundamental importance, understanding the microstructural response of CNC dispersions to shear is necessary in order to develop processing methodologies for producing coatings, films, and fibers with controlled properties.

Based on Table 1, three regions in the viscosity *versus* shear rate curves may exist over a much broader concentration range than previously thought based on visual inspection of the plots. However, it is difficult to conclude that these transitions are due to the classical three-region behavior caused by shear-induced changes in the motion of the individual mesogens or tactoids – individual chiral nematic domains. In the case of the biphasic 4.5 vol% dispersion, three regions could clearly be discerned (Fig. 3b), but even in this case the shear rate transitions between the region boundaries were not clear based on either visual inspection or numerical analysis. In the present work, the approximate onset of the region II plateau was 0.631 s^{-1} for the 3.83 vol% dispersion and generally shifted to lower shear rates as concentration increased the CNC/D_2O dispersions, taking place at approximately 0.398 s^{-1} for 4.50 vol% and 0.0398 s^{-1} for 5.16 vol%, and 0.0631 s^{-1} for 5.83 vol%. As for other rheological investigations of lyotropic nanocylinders dispersions,[39,52,53,55,70] the putative region II was not as flat or as broad as typically associated with lyotropic liquid crystalline polymers.[19,68] It should be noted however, that for some systems such as cholesteric hydroxypropyl cellulose (HPC) in water, the low and high shear rate regions (regions I and III) are separated by an inflection or hesitation point which is considered region II,[71] and not all lyotropic rod-like polymers exhibit three-region behavior.[68] At 6.50 vol% and above the low and high shear slopes are different (Table 1) however, there is not a clear transition point.

RheoSANS

Neutron scattering was used to quantify the microstructural changes that result from shear flow. To collect scattering data for the dispersions at rest, the samples were allowed to relax for up to 60 minutes after being loaded on the rheometer. Dispersions with $\phi \leq 5.83$ vol% exhibited isotropic scattering patterns after this relaxation time. As for other macromolecular lyotropic dispersions, the biphasic CNC dispersions had a polydomain texture; the individual domains each had a local director, but the sample was macroscopically isotropic.[23,58] Above 5.83 vol%, anisotropic scattering patterns were still observed after 60 min relaxation, due to slow relaxation kinetics and artifacts from the shear associated with loading the sample.[58] These samples were sheared at 0.01 s^{-1} to erase any remaining shear history.

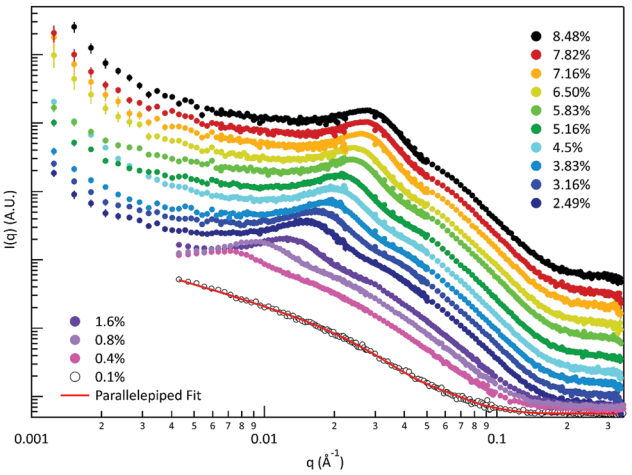

Fig. 4 Scattering curves for each CNC dispersion (vol%). For clarity, the intensities have been offset on the *y*-axis.

Scattering curves for each dispersion measured with rheoSANS prior to shear and for several lower concentration dispersions measured only at rest are shown in Fig. 4. As a note, the *q*-range probed for the dilution series and the rheoSANS are different because they were measured on different SANS instruments. Scattering from both individual particle "form factor" ($P(q)$) and interparticle interactions "structure factor" ($S(q)$) contribute to the overall scattering, such that the scattering intensity is proportional to the product of $S(q)$ and $P(q)$. When the concentration is sufficiently low and the interparticle interactions are negligible then $S(q)$ is equal to 1 and the scattering data is directly related to the average form factor of the particles in suspension. For the data presented here, only the 0.1 vol% sample is sufficiently dilute that the structure factor is negligible. As the CNC concentration increased a structure factor peak begins to emerge in the low q and shifts toward higher q with increasing concentration. This shift to higher q is expected as the dispersion becomes more concentrated and the characteristic distance separating nearest neighbor CNCs is reduced.

The 0.1 vol% dispersion data was fit with a parallelepiped model using SasView software.[72–75] Here we fixed the scattering length density of the CNC (1.9×10^{-6} A^{-2}),[75] the solvent (6.3×10^{-6} A^{-2}), and the length (163 nm from AFM) and fit the height (3.5 ± 0.06 nm), width (14.9 ± 0.15 nm), scale ($0.00072 \pm 9.2 \times 10^{-6}$), and incoherent background ($0.056 \pm 1.4 \times 10^{-4}$). The resulting fit is plotted as a line in Fig. 4 over the 0.1 vol% scattering data set. The width and height obtained by the fit are approximately half those measured by AFM. We suspect the discrepancy is due to a combination of potential aggregation during AFM sample preparation and neglecting to account for CNC polydispersity in the model fit.

Two-dimensional scattering data for the 2.49, 4.50, 7.16, and 8.48 vol% dispersions at selected shear rates $\dot{\gamma}$ are shown in Fig. 5.

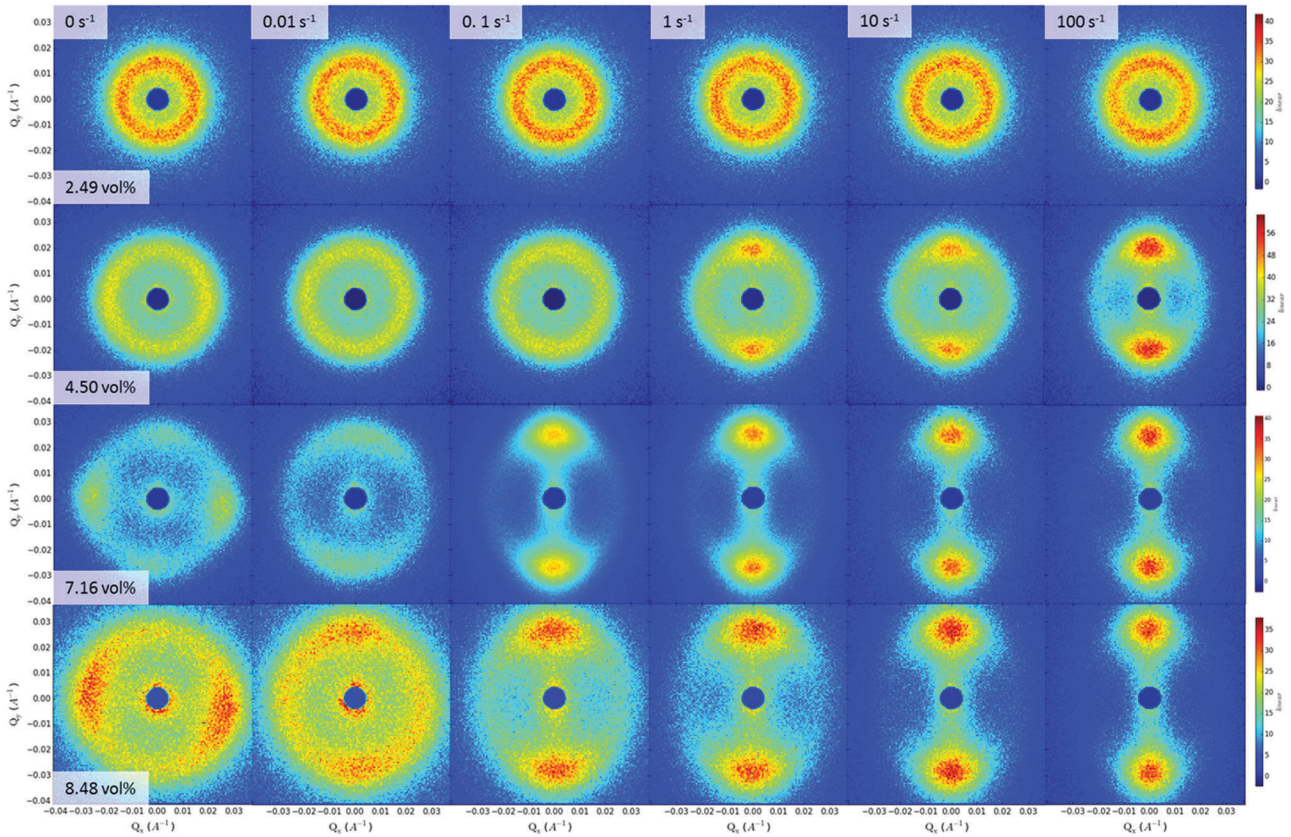

Fig. 5 Reduced two-dimensional scattering data for the 2.49, 4.50, 7.16, and 8.48 vol% dispersions at a range of shear rates between 0 and 100 s^{-1}.

As expected for a Newtonian fluid, the 2.49 vol% dispersion displayed an isotropic ring pattern at all shear rates. For the biphasic 4.50 vol% dispersion, anisotropy was seen in the scattering pattern beginning at $\dot{\gamma}$ = 0.158 s^{-1}, increased until $\dot{\gamma}$ = 1 s^{-1}, and then remained relatively constant at intermediate shear rates ($\dot{\gamma}$ = 1–10 s^{-1}). High intensity nodes were present perpendicular to the flow direction, while an isotropic ring was still visible. This suggests that while a portion of the rods aligned in the flow direction, some fraction of rods remained randomly oriented. At $\dot{\gamma}$ = 100 s^{-1} the scattering pattern was significantly more anisotropic with high intensity nodes perpendicular to the flow direction suggesting that the CNC were preferentially aligned in the flow direction. Little change was seen in the intensity of the isotropic ring from 1 to 10 s^{-1}, but the intensity decreased significantly from 10 to 100 s^{-1}. The 7.16 vol% rheological gel exhibited an anisotropic scattering pattern at 0 s^{-1} due to the previously described slow relaxation kinetics. However, at 0.01 s^{-1}, the residual anisotropic nodes were removed and the patterns were predominantly isotropic with slight alignment in the flow direction. At 0.1 s^{-1}, two high intensity nodes were observed perpendicular to the flow direction and little isotropic ring remained. Unlike the biphasic 4.50 vol% dispersion, the intensity of the remaining isotropic ring decreased steadily as the shear rate was increased from 0.1 to 100 s^{-1}. For the highest concentration sample, 8.48 vol% higher shear rates were required for to achieve significant anisotropy; this is consistent with the sample's higher elastic modulus and viscosity.

In order to quantify the overall degree of CNC alignment relative to the flow direction, an annular average was calculated for each 2D scattering pattern. The average was taken over a 0.0056 Å q range centered on the maximum intensity for each respective concentration. These annular averages were used to calculate the SANS order parameter $\bar{P}_2$ using the method presented by Burger *et al.*[76] Note that this a global (macroscopic) order parameter defined relative to the flow direction, and is not an equilibrium order parameter defined relative to a local director. The orientational distribution function $F(q,\phi)$, given by the annular averages are well fit by a Legendre series expansion:

$$F(q,\phi) = \sum_{n=0}^{\infty} a_n P_{2n}(\cos\phi) \quad (2)$$

where the values, a_n, are fitting coefficients and the functions, P_{2n}, are even Legendre Polynomials. The first six terms of the expansion were used to fit the annular averages. An example of the experimental annular averages and Legendre series fits are shown in Fig. 6. Order parameter $\bar{P}_2$ is directly related to the a_1 coefficient from the Legendre expansion.[76]

$$\bar{P}_2 = \frac{a_1}{5} \quad (3)$$

The value of $\bar{P}_2$ will vary from 0 for no macroscopic CNC orientation to 1 for CNC perfectly aligned in the flow direction.

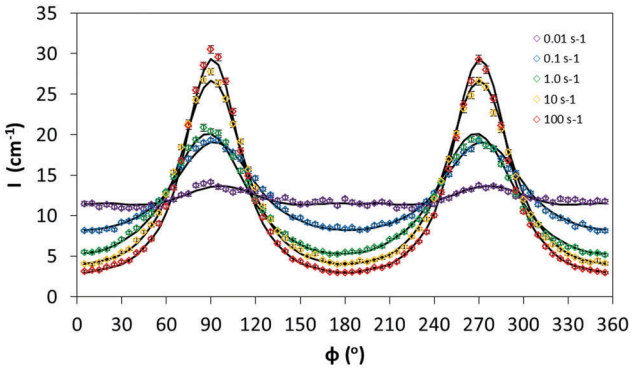

Fig. 6 Annular averages of 2D scattering patterns for 8.48 vol% CNC gel at shear rates ranging from 0.01 to 100 s^{-1}. Solid lines are Legendre expansion fits using eqn (1).

The order parameters were calculated for a range of CNC concentrations for 0.01 $s^{-1} \leq \dot{\gamma} \leq 100\ s^{-1}$.

Fig. 7a shows the calculated order parameters for samples ranging from 2.49 to 8.48 vol% over a range of shear rates. Fig. 7b shows that at 1 s^{-1}, the lowest shear rate for which data could be obtained for all concentrations, the viscosity and order parameter both increase with concentration until the gel transition at which point viscosity increases more slowly and the order parameter decreases. For the 2.49 and 3.16 vol% dispersions, which were either completely or predominantly isotropic, the SANS order parameter $\bar{P}_2 = 0$ until $\dot{\gamma} > 10\ s^{-1}$, and $\bar{P}_2 < 0.1$ even at $\dot{\gamma} = 100\ s^{-1}$ (Fig. 7a). This agrees well with the dispersions' nearly Newtonian rheological behavior. The 3.83 and 4.5 vol% biphasic samples showed nearly equivalent behavior with a steep increase in order parameter followed by a plateau from $1 < \dot{\gamma} < 10\ s^{-1}$ followed by another increase to 100 s^{-1}. The other biphasic samples (5.16 and 5.83 vol%) showed similar behavior, with an earlier onset of ordering and markedly higher order parameters at 100 s^{-1}. However the order parameter for the fully liquid crystalline (6.5 vol%) sample steadily increased with shear until approximately 10 s^{-1} and then begin to level off reaching a value of 0.47 at 100 s^{-1}. Interestingly, the lowest concentration rheological gel had the most rapid change in order parameter at low shear and then remained nearly flat with a final SANS order parameter of $\bar{P}_2 = 0.50$. Due to beamtime constraints, data were not obtained for all shear rates for the higher concentration gels, but it interesting that all the liquid crystalline and gel samples reached a similar value at 100 s^{-1}. The maximum SANS order parameter of 0.52 is much lower than those reported by Orts[58] and Ebeling[60] for liquid crystalline CNC dispersions in their respective RheoSANS and RheoSAXS studies. Orts reported an order parameter of 0.5 at only 3 s^{-1}; the order parameter increased to 0.75 at 100 s^{-1} and 0.92 at 7000 s^{-1}. The higher order parameter at 100 s^{-1} was likely due to their use of a fractionation procedure which reduced polydispersity and facilitated packing and alignment. The remarkably high value at 7000 s^{-1} highlights the high degree of alignment that can be achieved at high shear rates for samples with low polydispersity. Ebeling stated that order parameter in the flow direction increase from 0 at rest to 0.75 at 1700 s^{-1}, but did not provide values at intermediate shear rates or information on CNC size or polydispersity.[60]

Fig. 7c and d compare the biphasic dispersions' three-region order parameter behavior to their rheological behavior. For the biphasic dispersions, the viscosity *versus* shear rate plots only showed subtle transitions between power law regions. In contrast, plots of order parameter *versus* shear rate showed well-defined continuous three-region behavior. For each concentration, there was an initial increase in order parameter at low shear rate, followed by a nearly flat plateau at intermediate shear rates, and then a more rapid increase in order parameter at high shear rates. As expected, at a given shear rate the order parameter was higher for higher CNC concentrations. Table 2 shows the boundaries for each region, which were quantified by maximizing the R^2 value of linear fits. Interestingly, region I to region II order parameter transitions were at slightly higher shear rates than the transitions suggested by the viscosity data; and the region II plateaus persisted over a broader range of shear rates than the subtle transition regions in the viscosity *versus* shear rate plots. Also in contrast to the viscosity data, the breadth of the order parameter plateau increased with increasing concentration; this is more consistent with the behavior expected for classical lyotropic polymer systems where rheological three-region behavior occurs in fully liquid crystalline, not biphasic, dispersions. However, the origin of three-region behavior in the CNC system and the differences between the viscosity *versus* shear rate and order parameter *versus* shear rate behaviors need further investigation to be fully understood.

Based on the region II plateau being more pronounced in the biphasic than liquid crystalline dispersions as well as our previous rheo-optical investigations of CNC in H_2O,[42] we hypothesize that in region I the CNC liquid crystalline tactoids elongate and the directors are aligned in the flow direction. This would result in the observed increase in order parameter and corresponding decrease in viscosity. At the transition to region II, the liquid crystalline domains directors are oriented in the direction of shear, but the shear forces are not sufficient align the CNC in the isotropic phase. This would be consistent with the observation that biphasic dispersions at intermediate shear rates had scattering patterns that consisted of both anisotropic nodes and an isotropic ring. The transition from region II to region III is believed to be the shear rate that results in the CNC in the isotropic phase beginning to align in the flow direction. This is supported by 10 s^{-1} resulting in the slight increase in order parameter in the isotropic 3.16 vol% and the onset of region III in the biphasic 3.83 and 4.50 vol% dispersions (Table 2). As the shear rate is further increased in region III, the liquid crystalline and isotropic regions merge and the CNC are further aligned in the flow direction. The lower transition to region III for the higher concentration 5.16 and 5.83 vol% biphasic samples can be attributed to the concentration of rods in the isotropic phase increasing with overall concentration for this system of charged mesogens.[49]

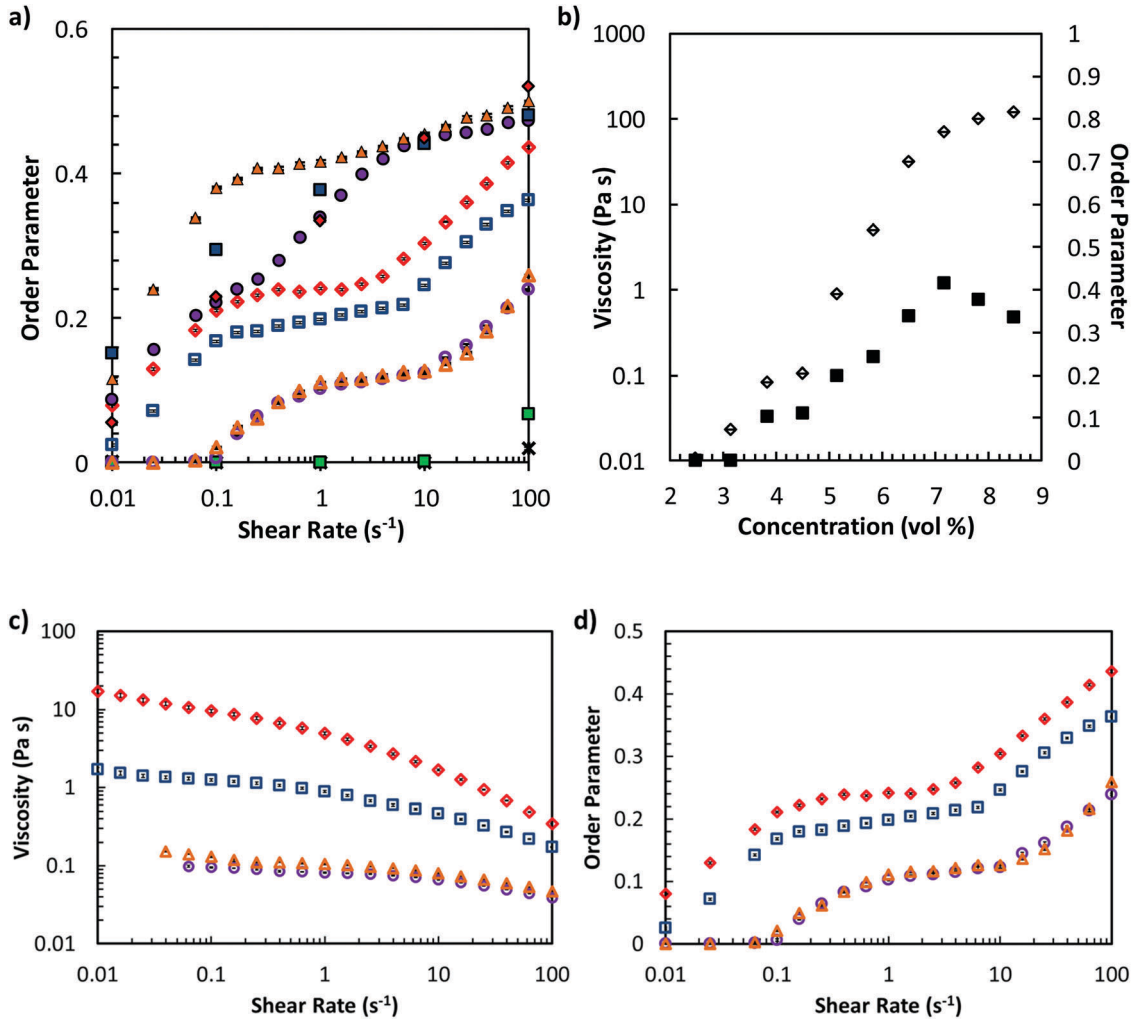

Fig. 7 (a) Order parameters relative to the flow direction for 2.49 (black stars), 3.16 (green squares), 3.83 (hollow purple circles), 4.5 (hollow orange triangles), 5.16 (hollow blue squares), 5.83 (hollow red diamonds), 6.5 (solid purple circles), 7.16 (solid orange triangles), 7.82 (solid blue squares), and 8.48 (solid red diamonds) vol%. (b) Viscosity (open diamonds) and order parameter (filled squares) at 1 s^{-1} as a function of concentration, (c) viscosity *versus* shear rate for biphasic samples (d) order parameter *versus* shear rate for the same samples.

Table 2 Shear rate (s^{-1}) at onset of region transitions for CNC dispersions from SANS data, based on acquisition of five data points per decade of shear

CNC conc. (vol%)	Onset of region II (s^{-1})	Onset of region III (s^{-1})
3.83	1.00	10.00
4.50	1.00	10.00
5.16	0.16	6.31
5.83	0.25	2.51

The potential for region II vorticity alignment[77] was also considered as a potential explanation for region II. However, scattering patterns collected in tangential beam alignment showed only isotropic rings, suggesting an absence of CNC vorticity alignment in contrast to the RheoSAXS investigation performed by Ebeling *et al.*[60]

In order to explore the above hypothesis for three-region behavior, rheo-optics was used to better visualize shear induced microstructural changes for the biphasic 4.50 vol% (Fig. 8). At $\dot{\gamma}$ = 1.0 s^{-1} the domains were clearly elongated in the flow direction, however, as indicated by bright birefringent domains at polarization angles of both 0° and 45°, the domain helix directors are not uniformly oriented in the flow direction. By $\dot{\gamma}$ = 1.0 s^{-1}, at the onset of region II, the 0° image shows significantly fewer birefringent domains than the 45° image, indicating that the domain directors are aligned in the direction of flow. Decreased domain size was also observed from 0.1 to 1.0 s^{-1}. This could explain the shift in the region transitions to lower shear rates in the viscosity curves, as viscosity is dependent on domain size while order parameter is not.[68] In region II ($\dot{\gamma}$ = 1.0–10 s^{-1}) some further domain breakup and alignment is observed, however in region III ($\dot{\gamma}$ = 10–100 s^{-1}) the liquid crystalline and isotropic domains are seen to fully merge into a monodomain aligned in the flow direction showing uniform optical texture which shows (full extinction at 0° and full birefringence at 45° cross polarized positions).

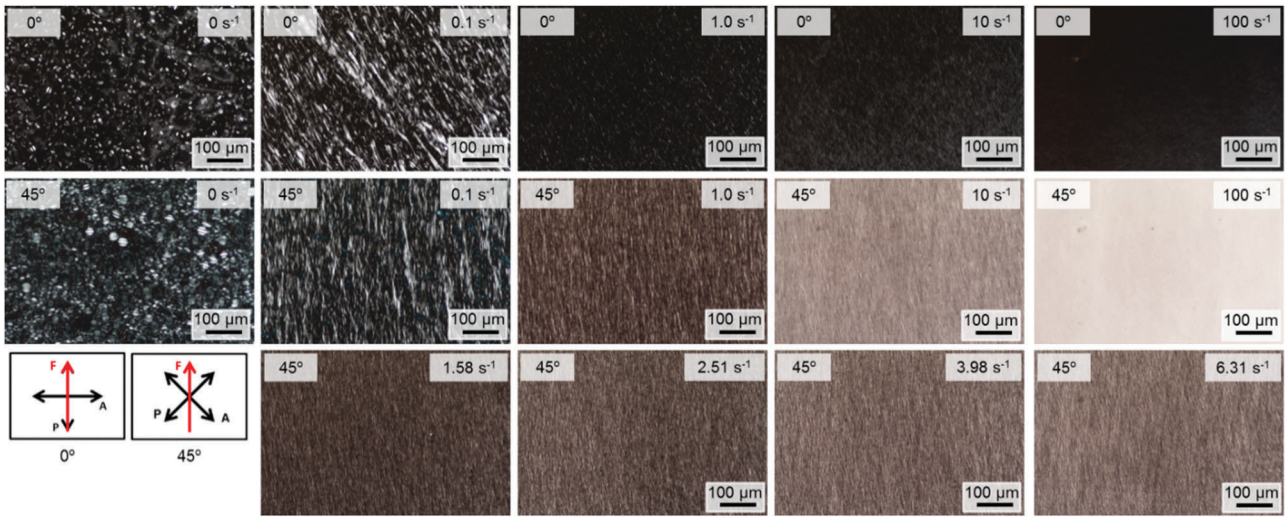

Fig. 8 Shear cell cross-polarized optical microscope images of the 4.50 vol% dispersion. The top two rows show the beginning of each decade of shear. In the top row, the flow direction is parallel to the polarization axis, on the middle row the flow direction is at 45° to the polarization axis. The bottom row shows additional images of region II behavior with the flow direction at 45° to the polarization axis.

Conclusion

RheoSANS was used to advance understanding of the effects of CNC concentration on rheological behavior and microstructural ordering. It identified distinct changes in the shear response of cholesteric CNC dispersions' microstructure between the isotropic, biphasic, liquid crystalline, and gel regimes. It confirmed that isotropic samples exhibit little shear induced ordering at shear rates up to 100 s^{-1}. However, biphasic samples have three distinct regions of shear response, which can be more readily identified by changes in SANS order parameter than by changes in viscosity. It is proposed that the origin of this three-region behavior is the result of differences between the shear response of the isotropic and liquid crystalline phases in the biphasic samples. Future research may further elucidate differences in spacing and ordering in these samples and the significant differences in shear-induced changes in order parameter between the biphasic and liquid crystalline samples.

Conflicts of interest

There are no conflicts to declare.

Acknowledgements

The authors acknowledge the collaborative National Science Foundation Grants CBET-1436637 and CBET-1437073, as well as IGERT DGE-1069004. This work utilized facilities supported in part by the National Science Foundation under Agreement No. DMR-1508249, and benefited from the use of the SasView application, originally developed under NSF award DMR-0520547. Certain commercial goods or equipment are identified herein in order to fully describe the experiment sufficiently. This does not imply an endorsement or recommendation by the National Institute of Standards and Technology.

References

1 J. P. F. Lagerwall and G. Scalia, *Curr. Appl. Phys.*, 2012, **12**, 1387–1412.
2 V. A. Davis, *J. Mater. Res.*, 2011, **26**, 140–153.
3 H. N. W. Lekkerkerker and G. J. Vroege, *Philos. Trans. R. Soc., A*, 2013, **371**, 2012063.
4 H. K. Bisoyi and S. Kumar, *Chem. Soc. Rev.*, 2011, **40**, 306–319.
5 J. M. Passantino, A. D. Haywood, J. Goswami and V. A. Davis, *Macromol. Mater. Eng.*, 2017, **302**, 1600351.
6 M. Bercea and P. Navard, *Macromolecules*, 2000, **33**, 6011–6016.
7 A. G. m Dumanli, H. M. van der Kooij, G. Kamita, E. Reisner, J. J. Baumberg, U. Steiner and S. Vignolini, *ACS Appl. Mater. Interfaces*, 2014, **6**, 12302–12306.
8 Y. Habibi, L. A. Lucia and O. J. Rojas, *Chem. Rev.*, 2010, **110**, 3479–3500.
9 I. Hoeger, O. J. Rojas, K. Efimenko, O. D. Velev and S. S. Kelley, *Soft Matter*, 2011, **7**, 1957–1967.
10 Y. Hu and N. Abidi, *Langmuir*, 2016, **32**, 9863–9872.
11 M.-C. Li, Q. Wu, K. Song, S. Lee, Y. Qing and Y. Wu, *ACS Sustainable Chem. Eng.*, 2015, **3**, 821–832.
12 M. Mariano, N. El Kissi and A. Dufresne, *J. Polym. Sci., Part B: Polym. Phys.*, 2014, **52**, 791–806.
13 C. Miao and W. Y. Hamad, *Cellulose*, 2013, **20**, 2221–2262.
14 H. Oguzlu, C. Danumah and Y. Boluk, *Curr. Opin. Colloid Interface Sci.*, 2017, **29**, 46–56.
15 J. H. Park, J. Noh, C. Schütz, G. Salazar-Alvarez, G. Scalia, L. Bergström and J. P. Lagerwall, *ChemPhysChem*, 2014, **15**, 1477–1484.
16 R. Rusli and S. J. Eichhorn, *Appl. Phys. Lett.*, 2008, **93**, 033111.
17 A. B. Reising, R. J. Moon and J. P. Youngblood, *J. Sci. Technol. For. Prod. Processes*, 2013, **2**, 32–41.
18 J. A. Diaz, X. Wu, A. Martini, J. P. Youngblood and R. J. Moon, *Biomacromolecules*, 2013, **14**, 2900–2908.

19 S. Onogi and T. Asada, *Rheology*, Springer, 1980, pp. 127–147.
20 J. Pan, W. Hamad and S. K. Straus, *Macromolecules*, 2010, **43**, 3851–3858.
21 J. H. Park, J. Noh, C. Schütz, G. Salazar-Alvarez, G. Scalia, L. Bergström and J. P. F. Lagerwall, *ChemPhysChem*, 2014, **15**, 1477–1484.
22 L. Onsager, *Ann. N. Y. Acad. Sci.*, 1949, **51**, 627–659.
23 G. Marrucci, in *Liquid Crystallinity in Polymers*, ed. A. Ciferri, VCH Publishers, New York, 1991, pp. 395–421.
24 M. Doi and S. F. Edwards, *The Theory of Polymer Dynamics*, Oxford University Press, Oxford, 1986.
25 G. Kiss and R. S. Porter, *J. Polym. Sci., Part C: Polym. Symp.*, 1978, 193–211.
26 G. Kiss and R. S. Porter, *J. Polym. Sci., Part B: Polym. Phys.*, 1980, **18**, 361–388.
27 G. Kiss and R. S. Porter, *J. Polym. Sci., Part B: Polym. Phys.*, 1996, **34**, 2271–2289.
28 G. Kiss and R. S. Porter, in *Mechanical and Thermophysical Properties of Polymer Liquid Crystals*, ed. W. Brostow, Chapman & Hall, London, 1998, pp. 342–406.
29 R. G. Larson, *The Structure and Rheology of Complex Fluids*, Oxford University Press, New York, 1999.
30 R. G. Larson and M. Doi, *J. Rheol.*, 1991, **35**, 539–563.
31 G. Marrucci and P. Maffettone, *J. Rheol.*, 1990, **34**, 1217–1230.
32 G. Marrucci and P. Maffettone, *J. Rheol.*, 1990, **34**, 1231–1244.
33 N. Grizzuti, S. Cavella and P. Cicarelli, *J. Rheol.*, 1990, **34**, 1293–1310.
34 J. F. Berret and D. C. Roux, *J. Rheol.*, 1995, **39**, 725–741.
35 J. F. Berret, D. C. Roux, G. Porte and P. Lindner, *EPL*, 1994, **25**, 521.
36 M. W. Liberatore, F. Nettesheim, P. A. Vasquez, M. E. Helgeson, N. J. Wagner, E. W. Kaler, L. P. Cook, L. Porcar and Y. T. Hu, *J. Rheol.*, 2009, **53**, 441–458.
37 M. Ripoll, P. Holmqvist, R. G. Winkler, G. Gompper, J. K. G. Dhont and M. P. Lettinga, *Phys. Rev. Lett.*, 2008, **101**, 168302.
38 J. Araki, M. Wada, S. Kuga and T. Okano, *Colloids Surf., A*, 1998, **142**, 75–82.
39 E. E. Urena-Benavides, G. Ao, V. A. Davis and C. L. Kitchens, *Macromolecules*, 2011, **44**, 8990–8998.
40 S. Shafiei-Sabet, W. Y. Hamad and S. G. Hatzikiriakos, *Langmuir*, 2012, **28**, 17124–17133.
41 Q. Wu, Y. Meng, S. Wang, Y. Li, S. Fu, L. Ma and D. Harper, *J. Appl. Polym. Sci.*, 2014, **131**, 40525.
42 A. D. Haywood and V. A. Davis, *Cellulose*, 2017, **24**, 705–716.
43 B. Derakhshandeh, G. Petekidis, S. Shafiei Sabet, W. Y. Hamad and S. G. Hatzikiriakos, *J. Rheol.*, 2013, **57**, 131–148.
44 S. Shafiei-Sabet, W. Hamad and S. Hatzikiriakos, *Cellulose*, 2014, **21**, 3347–3359.
45 S. Shafiei-Sabet, W. Y. Hamad and S. G. Hatzikiriakos, *Rheol. Acta*, 2013, **52**, 741–751.
46 J. Li, J. F. Revol and R. H. Marchessault, *J. Colloid Interface Sci.*, 1996, **183**, 365–373.
47 Z. Luo, H. Song, X. Feng, M. Run, H. Cui, L. Wu, J. Gao and Z. Wang, *Langmuir*, 2013, **29**, 12358–12366.
48 A. Stroobants, H. N. W. Lekkerkerker and T. Odijk, *Macromolecules*, 1986, **19**, 2232–2238.
49 X. M. Dong, T. Kimura, J. F. Revol and D. G. Gray, *Langmuir*, 1996, **12**, 2076–2082.
50 G. Lenfant, M.-C. Heuzey, T. G. M. van de Ven and P. J. Carreau, *Rheol. Acta*, 2017, **56**, 51–62.
51 C. Echeverria, P. L. Almeida, O. F. Aguilar Gutierrez, A. D. Rey and M. H. Godinho, *J. Polym. Sci., Part B: Polym. Phys.*, 2017, **55**, 821–830.
52 V. A. Davis, L. M. Ericson, A. N. Parra-Vasquez, H. Fan, Y. Wang, V. Prieto, J. A. Longoria, S. Ramesh, R. Saini, C. Kittrell, W. E. Billups, W. W. Adams, R. H. Hauge, R. E. Smalley and M. Pasquali, *Macromolecules*, 2004, **37**, 154–160.
53 G. Ao, D. Nepal and V. A. Davis, *Rheol. Acta*, 2016, **55**, 717–725.
54 T. Xu and V. A. Davis, *Langmuir*, 2014, **30**, 4806–4813.
55 S. Murali, T. Xu, B. D. Marshall, M. J. Kayatin, K. Pizarro, V. K. Radhakrishnan, D. Nepal and V. A. Davis, *Langmuir*, 2010, **26**, 11176–11183.
56 A. P. R. Eberle and L. Porcar, *Curr. Opin. Colloid Interface Sci.*, 2012, **17**, 33–43.
57 S. Förster, M. Konrad and P. Lindner, *Phys. Rev. Lett.*, 2005, **94**, 017803.
58 W. Orts, L. Godbout, R. Marchessault and J.-F. Revol, *Macromolecules*, 1998, **31**, 5717–5725.
59 W. J. Orts, L. Godbout, R. H. Marchessault and J. F. Revol, in *Flow-Induced Structure in Polymers*, American Chemical Society, 1995, vol. 597, ch. 23, pp. 335–348.
60 T. Ebeling, M. Paillet, R. Borsali, O. Diat, A. Dufresne, J. Cavaille and H. Chanzy, *Langmuir*, 1999, **15**, 6123–6126.
61 S. R. Kline, *J. Appl. Crystallogr.*, 2006, **39**, 895–900.
62 M. S. Reid, M. Villalobos and E. D. Cranston, *Langmuir*, 2017, **33**, 1583–1598.
63 T. Orlova, S. J. Aßhoff, T. Yamaguchi, N. Katsonis and E. Brasselet, *Nat. Commun.*, 2015, **6**, 7603.
64 A. M. Donald and A. H. Windle, *Liquid Crystalline Polymers*, Cambridge University Press, Cambridge, 2nd edn, 2006.
65 J. G. Kirkwood and R. J. Plock, *J. Chem. Phys.*, 1956, **24**, 665–669.
66 B. Lonetti, J. Kohlbrecher, L. Willner, J. K. G. Dhont and M. P. Lettinga, *J. Phys.: Condens. Matter*, 2008, **20**, 404207.
67 R. G. Larson, *The Structure and Rheology of Complex Fluids*, Oxford University Press, New York, 1999.
68 K. F. Wissbrun, *J. Rheol.*, 1981, **25**, 619–662.
69 G. Ao, D. Nepal, M. Aono and V. A. Davis, *ACS Nano*, 2011, **5**, 1450–1458.
70 T. Xu and V. A. Davis, *J. Nanomater.*, 2015, **16**, 447.
71 N. Grizzuti and P. L. Maffettone, *J. Chem. Phys.*, 2003, **118**, 5195–5200.
72 P. Mittelbach and G. Porod, *Acta Phys. Austriaca*, 1961, **14**, 185–211.
73 R. Nayuk and K. Huber, *Z. Phys. Chem.*, 2012, **226**, 837–854.

74 M. Doucet, J. H. Cho, G. Alina, S. King, P. Butler, P. Kienzle, J. Krzywon, A. Jackson, T. Richter, M. Gonzales, T. Nielsen, R. Ferraz Leal, A. Markvardsen, R. Heenan, P. Juhas, J. Bakker, P. Rozyczko, W. Potrzebowski, L. O'Driscoll, K. Campbell and A. Washington, *SasView Version 4.1.1*, Zenodo, 2017, DOI: 10.5281/zenodo.825675.

75 F. Cherhal, F. Cousin and I. Capron, *Biomacromolecules*, 2016, **17**, 496–502.

76 C. Burger, B. S. Hsiao and B. Chu, *J. Macromol. Sci., Part C: Polym. Rev.*, 2010, **50**, 91–111.

77 A. Montesi, A. A. Peña and M. Pasquali, *Phys. Rev. Lett.*, 2004, **92**, 058303.

